P 103 CIRCULATION AND AREAL CONTRACTION RATE AS DETECTED AND MEASURED BY DOPPLER RADAR

Vincent T. Wood and Robert P. Davies-Jones*
*Emeritus, NOAA/OAR/National Severe Storms Laboratory, Norman, Oklahoma

1. INTRODUCTION

Davies-Jones and Stumpf (1997) advocated using the detection and measurement of significant circulation around and areal contraction rate of a curve as a method for giving advanced warnings of tornadoes. Circulation (rate of areal contraction) is the line integral around a closed curve of velocity tangential (inward normal) to the curve. Circulation and areal contraction rate may be more useful than differential single-Doppler velocities in the characteristic velocity couplet for detecting and measuring the strength of convergent tornadic mesocyclones at low altitudes, because circulation and areal contraction rate are (a) less scale dependent, (b) more tolerant of noisy Doppler velocity data, (c) relatively insensitive to range and azimuth, beamwidth and location of a tornado within a sampling volume, as revealed by Davies-Jones and Stumpf (1997).

The objectives of the paper are (a) to derive mathematical formulas for calculating single-Doppler circulation and areal contraction rate of simulated convergent vortex flows, as sampled by a simulated phased-array radar, and (b) to investigate the effects of radar range and variable azimuthal beamwith on the calculated circulations and areal contraction rates of the flows.

2. 3-D VELOCITY COMPONENTS OF THE RADAR TARGETS

Since a Doppler radar normally scans in azimuth prior to changing elevation angle, it is expeditious and computationally economical to determine the kinematic properties of the velocity field in the conical surfaces of constant elevation angle. We define a right-handed spherical coordinate system (R, α, β) centered on the radar where R is the slant range, α is the elevation angle, and β is the azimuth angle measured clockwise from due north. The surface of constant elevation angle α_o is called henceforth the α_o-surface. In terms of Cartesian coordinates (x, y, z) where the radar is at the origin, the positive x- and y-axes are, respectively, directed towards the east and north in the plane tangent to the earth's surface and the z-axis points towards the zenith. The corresponding unit basis vectors are **i, j, k.** A radar target's position is given by

$$\mathbf{R} \equiv \begin{bmatrix} x \\ y \\ z \end{bmatrix} = \begin{bmatrix} R\cos\alpha\sin\beta \\ R\cos\alpha\cos\beta \\ R\sin\alpha \end{bmatrix}, \qquad (2.1)$$

Corresponding author address: Vincent T. Wood, National Severe Storms Laboratory, 120 David L. Boren Blvd., Norman, Oklahoma 73072, USA; e-mail: Vincent.Wood@noaa.gov

where $\mathbf{R} = R\cos\alpha\sin\beta\,\mathbf{i} + R\cos\alpha\cos\beta\,\mathbf{j} + R\sin\alpha\,\mathbf{k}$, and the spherical coordinates are related to the Cartesian coordinates by $R = |\mathbf{R}| = \sqrt{x^2+y^2+z^2}$, $\alpha = \sin^{-1}(z/R)$, and $\beta = \tan^{-1}(x/y)$. The 3-d vector velocity of the targets, $\mathbf{V} = \dot{\mathbf{R}} \equiv d\mathbf{R}/dt$, is

$$\mathbf{V} = \begin{bmatrix} \cos\alpha\sin\beta \\ \cos\alpha\cos\beta \\ \sin\alpha \end{bmatrix}\dot{R} + \begin{bmatrix} -\sin\alpha\sin\beta \\ -\sin\alpha\cos\beta \\ \cos\alpha \end{bmatrix} R\dot{\alpha} + \begin{bmatrix} \cos\beta \\ -\sin\beta \\ 0 \end{bmatrix} R\cos\alpha\,\dot{\beta}\,, \qquad (2.2)$$

$$= \dot{R}\hat{\mathbf{R}} + R\dot{\alpha}\hat{\boldsymbol{\alpha}} + R\cos\alpha\dot{\beta}\hat{\boldsymbol{\beta}}\,,$$

where $\dot{R} \equiv \frac{dR}{dt}$, $\dot{\alpha} \equiv \frac{d\alpha}{dt}$, and $\dot{\beta} \equiv \frac{d\beta}{dt}$; an overdot denotes differentiation with respect to time t. The unit basis vectors ($\hat{\mathbf{R}}$, $\hat{\boldsymbol{\alpha}}$, $\hat{\boldsymbol{\beta}}$) of the spherical coordinate system are given by

$$\hat{\mathbf{R}} = \left|\frac{\partial\mathbf{R}}{\partial R}\right|^{-1}\frac{\partial\mathbf{R}}{\partial R} = \begin{bmatrix} \cos\alpha\sin\beta & 0 & 0 \\ 0 & \cos\alpha\cos\beta & 0 \\ 0 & 0 & \sin\alpha \end{bmatrix}\begin{bmatrix} \mathbf{i} \\ \mathbf{j} \\ \mathbf{k} \end{bmatrix}$$

$$\hat{\boldsymbol{\alpha}} = \left|\frac{\partial\mathbf{R}}{\partial\alpha}\right|^{-1}\frac{\partial\mathbf{R}}{\partial\alpha} = \begin{bmatrix} -\sin\alpha\sin\beta & 0 & 0 \\ 0 & -\sin\alpha\cos\beta & 0 \\ 0 & 0 & \cos\alpha \end{bmatrix}\begin{bmatrix} \mathbf{i} \\ \mathbf{j} \\ \mathbf{k} \end{bmatrix}, \qquad (2.3)$$

and $\hat{\boldsymbol{\beta}} = \left|\frac{\partial\mathbf{R}}{\partial\beta}\right|^{-1}\frac{\partial\mathbf{R}}{\partial\beta} = \begin{bmatrix} \cos\beta & 0 & 0 \\ 0 & -\sin\beta & 0 \\ 0 & 0 & 0 \end{bmatrix}\begin{bmatrix} \mathbf{i} \\ \mathbf{j} \\ \mathbf{k} \end{bmatrix}$,

where, $\hat{\mathbf{R}}$ is in the direction of increasing slant range, $\hat{\boldsymbol{\alpha}}$ is in the direction of increasing elevation angle, and $\hat{\boldsymbol{\beta}}$ is in the direction of increasing azimuth. From (2.2) and (2.3), we obtain

$$\mathbf{V} = V_R\hat{\mathbf{R}} + V_\alpha\hat{\boldsymbol{\alpha}} + V_\beta\hat{\boldsymbol{\beta}}\,, \qquad (2.4)$$

where $V_R = \dot{R}$, $V_\alpha = R\dot{\alpha}$, and $V_\beta = R\cos\alpha\,\dot{\beta}$. The dot product of (2.4) with $\hat{\mathbf{R}}$ is the Doppler velocity component V_R. The other components V_α and V_β are unobserved because they are perpendicular to the radar viewing direction. In the formulas derived below, the observed parts of the quantities are obtained by setting the unobserved velocity components to zero (i.e., ignoring them). At 0^o elevation angle, the formulas for the observed parts of a vertical vorticity and shearing deformation are identical (apart from sign) and those for divergence and stretching deformation are very similar. Thus, there is no way to distinguish vorticity from shearing deformation and divergence from stretching deformation with a single Doppler radar (e.g., Peace et al. 1969). In the subsequent sections, we will develop the formulas for circulation and vorticity that represent a local rotational flow and also for areal contraction (expansion) rate and convergence (divergence) that represent a local convergent (divergent) flow, as measured by a single Doppler radar.

3. PHASED-ARRAY RADAR

The research S-band phased-array radar (PAR) is located at the National Weather Radar Testbed in north part of Norman, Oklahoma and is part of the broader

multifunction PAR initiative that is investigating the use of a single radar system to perform both weather and aircraft surveillance functions (Weber et al. 2007; National Academies 2008). The PAR consists of a WSR-88D transmitter; the antenna consists of 4352 radiating elements that, when the beam is normal to the face, produce a half-power beamwidth of 1.5° (BW_o). The half-power beamwidth (BW, hereafter simply referred to as beamwidth) increases to 2.1° when the antenna electronically scans ±45° angles from the perpendicular. The electronic scanning of the single antenna covers only one-quarter of the full 360° wide azimuthal coverage region of WSR-88D. Interested readers may refer to Zrnić et al. (2007) for a detailed technical description of the PAR and Heinselman et al. (2008) and Heinselman and Torres (2011) for high-temporal-resolution capabilities of the radar.

In our PAR simulation study, PAR velocity data are recorded on constant α_o-surfaces at grid points with constant radial spacing ΔR. The increment in elevation angle between each azimuthal scan is variable. The indices i, k are used to label the range and azimuth of grid points. Thus, the grid points in a surface of constant elevation α_o are located at (R_i, α_o, β_k) where $R_i = i\Delta R$. $\Delta R =$ 240 m is used. The i, k grid cell is defined as the area in the surface enclosed by successive range gates R_i and R_{i+1} and successive radials β_k and β_{k+1}. If the sector scan being analyzed includes due north, we add 360° to the azimuths east of north to make β continuous across the sector.

The azimuthal spacing is variable for PAR data. The BW varies azimuthally along each face according to

$$\frac{BW}{BW_o} = \sec(\beta - \phi_n) \,, \qquad (3.1)$$

where BW_o is the broadside beamwidth of 1.5°, and ϕ_n is the broadside azimuth of the face (Brown and Wood 2012). The broadside azimuths of the N (≥ 3) faces are given by

$$\phi_n = \phi_o + \frac{2n\pi}{N} \,, \; n = 0, 1, \ldots, N\text{-}1 \,, \qquad (3.2)$$

where n is the face number. We match the grid with the variable BW by letting the grid azimuth spacing vary in proportion to the BW. The grid azimuths also should include the broadside azimuths and the transitional azimuths between faces. To find grid azimuths that satisfy these conditions, we let

$$d\beta = \sec(\beta - \phi_n)\, d\mu \,, \qquad (3.3)$$

along the n^{th} face where $d\mu$ is a constant and the angles are in radians. The integral of (3.3) with $\mu = 0$ at broadside is given by

$$\mu = \sin(\beta - \phi_n) \,. \qquad (3.4)$$

The ranges of β and μ on each face are $\phi_n \pm \pi/N$ and $\pm \sin(\pi/N)$, respectively. We divide the range of μ into $2M$ equally spaced intervals with

$$M = \frac{1}{d\mu} \sin\left(\frac{\pi}{N}\right) \qquad (3.5)$$

and grid points in μ-space at

$$\mu_m = m\, d\mu, \; m = -M, -M+1, \ldots, -1, 0, 1, \ldots, M-1, M \,. \qquad (3.6)$$

The associated azimuths are

$$\beta_{m,n} = \phi_n + \sin^{-1}\left(\frac{m}{M} \sin\frac{\pi}{N}\right) . \qquad (3.7)$$

There are $2M + 1$ grid azimuths per face. Note that $\beta_{M,0} = \beta_{-M,1}$, etc. Therefore, there are $2MN$ total azimuths (because the N transitional azimuths between faces are counted only once). We let $d\mu = BW_o/c$ where c is a constant. From (3.3) and (3.1), we see that

$$d\beta = \frac{BW}{c} \,. \qquad (3.8)$$

Because M is an integer, it is apparent from (3.5) that BW_o/c must divide $\sin(\pi/N)$. Otherwise, c is arbitrary.

For the PAR advocated by Brown and Wood (2012), the variable azimuth spacing ($d\beta$) is 0.75° at broadside increasing to 1.06° at the transitional azimuths (Fig. 1), $N = 4$, and $\phi_o = 45°$. Thus, the broadside azimuths are 45°, 135°, 225°, and 315° and the transitional azimuths are 0°, 90°, 180°, and 270°. For the Testbed PAR $BW_o = 1.5°$, $c = 2$, $M = 54$, with 50% azimuthal overlapping. This yields a total of $2M + 1 = 109$ beam positions per 90° azimuthal sector at each elevation angle (Torres et al. 2013). If $BW_o = 1.0°$ were used, there would be a total of $2M + 1 = 163$ beam positions with $d\beta = 0.5°$ at broadside and $BW = 1.414°$ and $d\beta = 0.71°$ at the transitional azimuths of $\phi_o \pm 45°$ (Fig. 1).

Since our research PAR currently has only one flat-face antenna, the antenna rotates to a broadside azimuth that allows coverage of the 90° wide sector of interest and then remains stationary during data collection until the storms of interest move toward the edge of the sector. We arbitrarily chose the broadside azimuth $\phi_o = 0°$ (facing north) in (3.2) so that the transitional azimuths are ±45°. Then, (3.7) becomes

$$\beta_{m,o} = \sin^{-1}\left(\frac{m}{54} \sin\frac{\pi}{4}\right) , \; \beta_{m,o} \le \pm 45° \,. \qquad (3.9)$$

In section 6, we can scan a simulated Testbed PAR across convergent vortices. The vortices represent mesocyclones and tornadoes embedded in a convergent flow. Apart from a generalization to allow variable azimuth spacing, the simulator is the same as the one used by Davies-Jones and Wood (2006). We assume that the radar measurements are free of noise to avoid the complications of interpretation in the simulated Doppler velocity fields.

4. CIRCULATION AND VORTICITY

By Stokes' theorem, circulation and vorticity are related by

$$\Gamma = \oint_C \mathbf{V} \cdot d\mathbf{l} = \iint_A \boldsymbol{\omega} \cdot \mathbf{n}\, dA \,, \qquad (4.1)$$

where the vector element $d\mathbf{l}$ is tangential to the circuit. Here, the circulation Γ about a closed circuit C in a fluid, defined as the line integral about the circuit of the tangential component of vector velocity $\mathbf{V}$, is equal to the integral over the enclosed area A of the component of vector vorticity $\boldsymbol{\omega}$ along the outward normal $\mathbf{n}$ to the area A.

The relative vorticity normal to the α_o-surface is given by

$$\omega_\alpha \equiv (\nabla \times \mathbf{V}) \cdot \hat{\boldsymbol{\alpha}} = \frac{1}{R \cos\alpha_o} \frac{\partial V_R}{\partial \beta} - \frac{1}{R} \frac{\partial}{\partial R}\left(R V_\beta\right) . \qquad (4.2)$$

The minus sign in (4.2) arises because β increases in the clockwise direction. The term $\frac{1}{R\cos\alpha_o}\frac{\partial V_R}{\partial \beta} - \frac{\partial V_\beta}{\partial R}$ represents the shear vorticity of the radar's target; $-\frac{V_\beta}{R}$ is the curvature vorticity. The circulation Γ around the

boundary C of an area A in the α_o-surface is obtained from (4.1) and (4.2), via Stokes' theorem, as follows:

$$\Gamma = \cos\alpha_o \iint_A \omega_\alpha R dR d\beta = \iint_A \frac{\partial V_R}{\partial \beta} d\beta dR - \cos\alpha_o \iint_A \frac{\partial}{\partial R}(RV_R) dR d\beta \,, \quad (4.3)$$
$$= \oint_C (V_R dR + V_\beta R \cos\alpha_o d\beta) \,.$$

The mean vorticity in A in the direction perpendicular to the α_o-surface is Γ/A. Multiplying this quantity by $\cos\alpha_o$ gives its contribution to the mean vertical vorticity $\overline{\zeta}$ in A.

By ignoring V_β in (4.3), we obtain the observed circulation Γ_{ob} around the boundary C. It is given by

$$\Gamma_{ob} = \oint_C V_R dR \,. \quad (4.4)$$

Thus, the "cell circulation" Γ_{ob} around the i,k grid cell, assigned to the midpoint of each cell for plotting purposes, is

$$\left(d\Gamma_{i+1/2,k+1/2}\right)_{ob} = \frac{\Delta R}{2}[V_R(R_i,\alpha_o,\beta_{k+1}) + V_R(R_{i+1},\alpha_o,\beta_{k+1}) - V_R(R_{i+1},\alpha_o,\beta_k) - V_R(R_i,\alpha_o,\beta_k)] \,, \quad (4.5)$$

where i is the index in the range direction, k is the index in the azimuth direction, and $\Delta R = R_{i+1} - R_i$ is the range increment. Circulation is additive (Petterssen 1956, p. 127; Hess 1959, p. 210). The circulation around the outer perimeter of a union of contiguous grid cells is simply the sum of the circulations around the perimeter of each grid cell.

Computing the observed circulation around a smooth circular contour of fixed radius ρ in the α_o-surface provides a more precise standardized measure of circulation for indicating the trend of a moving mesocyclone's intensity or for comparing the strengths of different mesocyclones or tornadic vortex signatures. For an accurate assessment of circulation, ρ should be greater than the azimuthal spacing (in km) at the range of the vortex.

We have designed a circulation algorithm. First, we estimate the point (R_c, α_o, β_c) where the axis of the mesocyclone, intersects the conical α_o-surface. We then compute the intersection of the cone with a sphere with center at (R_c, α_o, β_c) and a radius ρ ($< R_c$) that is appropriate for mesocyclones and smaller vortices (ρ may be varied from 0.5 to 6 km in separate runs of the algorithm). We thus obtain a closed smooth contour that is "circle-like" (Fig. 2), because it consists of points that are equally distant in three-dimensional space from the mesocyclone center. The equation of the cone is Eq. (2.1) with α replaced by α_o, and the equation of the sphere is

$$(x - R_c\cos\alpha_o\sin\beta_c)^2 + (y - R_c\cos\alpha_o\cos\beta_c)^2 + (z - R_c\sin\alpha_o)^2 = \rho^2 \,. \quad (4.6)$$

They intersect on the closed curve

$$R^2 - 2RR_c[\cos(\beta - \beta_c)\cos^2\alpha_o + \sin^2\alpha_o] + R_c^2 = \rho^2. \quad (4.7)$$

This curve encloses an area $A = \pi\rho^2\sec\alpha_o$ in the surface. The projection of this curve onto the 0° elevation angle is a true circle of radius ρ. We exclude the case where some of the circle (other than a small arc) lies outside the analysis region and the case where the radar lies inside the circle. By symmetry, the points on the contour that are nearest to and furthest from the radar lie on the β_c radial. Hence, the ranges of points along the contour lie in the interval $[R_c - \rho, R_c + \rho]$. The circulation around this contour then can be computed as follows. Define M uniformly spaced range circles

$$R_m = R_c - \rho + \left(\frac{2m-1}{M}\right)\rho \,, \quad m=1, 2,\ldots,M. \quad (4.8)$$

all of which intersect the contour at two points (Fig. 2). Note that m and M here are different from the m and M in section 3. The range circles include all those in the grid plus intermediate ones if needed for greater accuracy. We add the four points

$$(R_c \pm \rho, \alpha_o, \beta_c), (R_T, \alpha_o, \beta_C \pm \beta_T) \,, \quad (4.9)$$

where $R_T = \sqrt{R_c^2 - \rho^2\sec^2\alpha_o}$ is the range tangent to C and $\beta_T = \sin^{-1}\left(\frac{\rho}{R_c\cos\alpha_o}\right)$ is the angle at which R_T is tangent to C. In (4.9), these points are the intersection of C and the radial through the vortex axis and the points where radials are tangent to C (Fig. 2). The $2M$+4 points are sequenced in a counterclockwise chain around C. We then use bilinear interpolation to calculate the Doppler velocity at each point in the chain. For accurate calculations, the number of interpolation points should be about 60.

We compute the circulation around C by the line-integral method (Davies-Jones 1993). This method fits a piecewise-linear velocity field to the observation (linear between adjacent points on the circle). The formula is given by

$$\Gamma = \frac{\Lambda(V_R,R)}{2} - \cos\alpha_o\frac{\Lambda(RV_\beta,\beta)}{2} \,, \quad (4.10)$$

where

$$\Lambda(f,g) \equiv (f_1g_2 - f_2g_1 + f_2g_3 - f_3g_2 + \cdots + f_{2M+3}g_{2M+4} - f_{2M+4}g_{2M+3} + f_{2M+4}g_1 - f_1g_{2M+4}) \,. \quad (4.11)$$

The first (second) term on the right-hand side of (4.10) is the observed (unobserved) circulation.

5. AREAL CONTRACTION RATE AND CONVERGENCE

Saucier (1955) showed that horizontal divergence is fractional areal expansion per unit time of the fluid element, given by

$$\delta \equiv \frac{\partial u}{\partial x} + \frac{\partial v}{\partial y} = \frac{1}{A}\frac{dA}{dt} \,, \quad (5.1)$$

where u, v are the eastward and northward components of horizontal flow, A is the horizontal area of the fluid element, and $dA/dt \equiv A_t > 0\ (< 0)$ is the rate at which the projected area of the curve expands (contracts). Sikdar et al. (1970), Mack and Wylie (1982), and Machado and Laurent (2004) used the areal expansion rate in (5.1) to make upper-level wind divergence or cloud measurements using satellite data. Rapid area expansion corresponds to large upper-level wind divergence (e.g., Wallace and Hobbs 1977, p. 400). Davies-Jones (1993) used the areal expansion rate to compute divergence from a triangle of wind sensors with the assumption of a linear wind field. Davies-Jones and Stumpf (1997) estimated the circulations and areal contraction rates of Doppler velocity signatures around circles of 2-km radius centered on the signatures. Davies-Jones and Wood (2006) used a virtual Doppler radar and a model of a vortex that contracted into a tornado to show that high circulation and convergence

values gave an early warning of imminent tornadogenesis.

For Doppler radial velocity application, we adapt (5.1) so that the equation becomes the divergence in a constant α_o-surface. It is given by

$$\delta = \frac{1}{A}\frac{dA}{dt}\,, \qquad (5.2)$$

where the element of area dA on the α_o-surface (Hildebrand 1962, p. 304) is

$$dA = \cos\alpha_o R\, dR\, d\beta\,. \qquad (5.3)$$

The area of the i,k grid cell is given as

$$A_{i+1/2,k+1/2} = \frac{1}{2}\cos\alpha_o\left(R_{i+1}^2 - R_i^2\right)(\beta_{k+1} - \beta_k)\,. \quad (5.4)$$

Let $r = R\cos\alpha_o$ be the horizontal range, A be the signed area enclosed by a curve C in the α_o-surface, and $A_o = A\cos\alpha_o$ and C_o be the projections of A and C onto a horizontal plane. Using the formula for the area of a plane region in polar coordinates (Kreyzig 1972, p. 339), we have

$$A_o = -\frac{1}{2}\oint_{C_o} r^2 d\beta\,, \qquad (5.5)$$

where A_o is positive when C_o is traversed counter-clockwise. Hence,

$$A = -\frac{1}{2}\cos\alpha_o \oint_C R^2 d\beta\,. \qquad (5.6)$$

The minus signs in (5.5) and (5.6) arise because β increases in the clockwise direction.

Differentiating (5.6) with respect to time t and integrating by parts give the rate of areal expansion (the negative of the areal contraction rate) on the α_o-surface,

$$A_t = -\cos\alpha_o \oint_C V_R R d\beta + \oint_C V_\beta dR\,, \qquad (5.7)$$

where the first and second terms on the right-hand side of (5.7) are the observed and unobserved effluxes, respectively.

In the last part of section 4, we defined a quasi-circular curve C and a chain of interpolation points on C. By the line-integral method of Davies-Jones (1993), the expansion rate of the area A enclosed by C is

$$A_t = -\cos\alpha_o \frac{\Lambda(RV_R,\beta)}{2} + \frac{\Lambda(V_\beta,R)}{2}\,, \qquad (5.8)$$

where the last term on the right-hand side of (5.8) is unobserved. A large positive observed contraction rate, for example, would be a strong indication that a mesocyclone or tornado is spinning up rapidly.

By ignoring the last term on the right-hand side of (5.7), we obtain the observed expansion rate of the i,k grid cell (again plotted at the midpoint of the cell)

$$\left(\frac{dA_{i+1/2,k+1/2}}{dt}\right)_{ob} = \frac{1}{2}\cos\alpha_o\,(\beta_{k+1} - \beta_k)\{R_{i+1}[V_R(R_{i+1},\alpha_o,\beta_{k+1}) + V_R(R_{i+1},\alpha_o,\beta_k)] - R_i[V_R(R_i,\alpha_o,\beta_{k+1}) + V_R(R_i,\alpha_o,\beta_k)]\}\,. \qquad (5.9)$$

In (5.9), the observed areal expansion rate of a union of contiguous grid cells is the sum of the areal expansion rates of the individual cells.

6. SIMULATION STUDY

6.1 Rankine Model

Simulated Doppler velocities were produced by scanning a simulated PAR radar across the Rankine vortical and convergent flows. The discrete Doppler velocity component at lower elevation angles is expressed by

$$V_R(R_i,\alpha_o,\beta_k) = (U\sin\gamma + V\cos\gamma)\cos\alpha_o, \qquad (6.1)$$

where U is the radial component of an axisymmetric convergent flow, V is the tangential component of an axisymmetric cyclonic vortex, and $\gamma(=\theta+\beta_k)$ is the angle between the tangential direction component V and the radar viewing direction β_k at a point. Here, θ is the angle between east and the radial direction from the flow feature center (positive in a counterclockwise direction). In (6.1), U and V can be modeled using the Rankine (1882) formulas to represent an idealized vortex embedded in an idealized convergent flow region at a low altitude. They are given by

$$U = U_x\left(\frac{\rho}{R_x}\right)^{\varepsilon}\,, \qquad (6.2a)$$

and

$$V = V_x\left(\frac{\rho}{R_x}\right)^{\varepsilon}\,, \qquad (6.2b)$$

where U_x and V_x are, respectively, the radial and tangential velocity peaks, ρ is the radius from the flow feature center, and R_x is the core radius at which the velocity peak occurs. The exponent ε=1 governs the inner velocity profile within the core region ($\rho \le R_x$) and ε=-1 is another exponent that governs the outer velocity profile beyond the core region ($\rho > R_x$).

6.2 Discussion

We simulated the Doppler velocity field that a PAR would see as it scanned an axisymmetric vortex in the above convergent axisymmetric flow (Fig. 3). The vortex's center is located at 25 km north of the radar and centered at the broadside azimuth of 0°. The input parameters in (6.2) for constructing the radial profiles of assumed Rankine radial and tangential velocities (m s^{-1}) are: (a) U_x=-25 and V_x=0, (b) U_x=-17.7 and V_x=17.7, and (c) U_x=0 and V_x=25. Their assumed core radii (R_x) are 2.5 km. We find the sensitivities of circulations, areal contraction rates, and other parameters to range and azimuth by varying the locations of the flow axis in our simulations.

The two-dimensional contouring technique of Bourke (1987) was chosen for analysis, rather than an objective analysis scheme, in order for radar data to be displayed in their original spherical coordinate system without altering the peak Doppler velocity values (Fig. 4d-f). Thus, the extreme velocity values of the high-resolution PAR data were preserved within and surrounding the convergent vortex signatures. The Doppler velocity contours (Figs. 3d-f) correspond to the 2-d horizontal wind fields (Figs. 3a-c). The Doppler velocity pattern rotates counterclockwise, reflecting a change from (a) convergent flow without the presence of rotation (Figs. 3a, d) through (b) combined convergence and rotation (Figs. 3b, e) to (c) rotational flow without the presence of convergence (Figs. 3c, f).

Cell circulations and cell areal contraction rates are calculated and plotted in Fig. 4. A potential vortex (the outer part of the Rankine vortex) and a sink each produce spurious "quadrupole" patterns in both the observed parts of vertical vorticity and of horizontal divergence, as observed by the Doppler radar. These patterns feature false readings outside the Rankine core

region (see Fig. 4). As the Doppler velocity pattern rotates counterclockwise from Fig. 3d through Fig. 3e to Fig. 3f, the quadrupole patterns change drastically (Fig. 4), and changes in the observed vorticity and convergence are also evident inside the core region ($\rho \le R_x$).

For a circle centered on the vortex (e.g., Fig. 2), the quadrupole contributions to circulation and areal contraction rate cancel. For circles of radii 0.5, 1.0, 1.5, …, 5.0 km centered on the vortex signature center, the computed circulations (red dotted curves) and areal contraction rates (blue dotted curves) are plotted as functions of circle radius in Fig. 5. From (4.1), the circulation at radius ρ is

$$\Gamma_m = \oint V d\rho = 2\pi V\rho \qquad (6.3)$$

Since the observed circulation is nearly one half of the model circulation (Γ_m) in (6.3), we divide (6.3) by 2. We then substitute (6.2b) into (6.3). Thus, the observed circulation of the flow is

$$\Gamma_m = \pi V\rho = \begin{cases} \pi V_x \frac{\rho^2}{R_x}, & \rho \le R_x \\ \pi V_x R_x, & \rho > R_x \end{cases}. \qquad (6.4)$$

In a manner similar to the development of (6.4), the model areal expansion rate (A_{t_m}) is obtained by differentiating a circular area ($A = \pi\rho^2$) with respect to time. It is given by

$$A_{t\_m} = 2\pi\rho\rho_t = 2\pi U\rho = \begin{cases} 2\pi U_x \frac{\rho^2}{R_x}, & \rho \le R_x \\ 2\pi U_x R_x, & \rho > R_x \end{cases}, \qquad (6.5)$$

where $U \equiv \rho_t$ is the radial component of flow diverging from its source. Dividing (6.5) by 2 yields approximately one half of the model areal contraction rate ($A_{t\_m} < 0$ since $U_x < 0$):

$$A_{t\_m} = \begin{cases} \pi U_x \frac{\rho^2}{R_x}, & \rho \le R_x \\ \pi U_x R_x, & \rho > R_x \end{cases}. \qquad (6.6)$$

Inside the core ($\rho \le R_x$), circulation and areal contraction rate vary as ρ^2. From the core wall to radial infinity, both circulation and areal contraction rate are constant.

The model radial profiles of Γ_m and A_{t_m} are plotted in Fig. 5, alongside the radial profiles of the simulated observed circulations and areal contraction rates. The agreement between the actual and observed profiles is excellent everywhere except near the core wall, where the cusp in the velocity profile at the core wall is smoothed but degraded, owing to the Doppler velocities being weighted means over 3-d sampling volumes. Therefore, the core radius is quite accurately measured, but the observed peak velocity is slightly undervalued at 25-km range. Beyond R_x, the observed areal contraction rates (circulations) approach rapidly the asymptotes, which are the conserved values of A_{t_m} (Γ_m). Note that the radial profiles of circulations (e.g., Figs. 5b, c) are the mirror images of those profiles of areal contraction rates (e.g., Figs. 5d, e).

We also compare the Doppler velocity fields in the cases, where the signature centers are at broadside (0º) and transitional (45º) azimuths at 25-km range (Fig. 6). For a given BW_o of 1.5º, the BW increases to 2.12º at the transitional azimuth, and the variable azimuth interval ($d\beta$) increases from 0.75º at the broadside azimuth to 1.06º at the transitional azimuth. Figs. 6c, f as well as Table 1 show that the Doppler velocity patterns of the vortex signature do not change much with the increasing beamwidth. At short range, the transitional beamwidth is sufficient to resolve the mesocyclone well.

There is also no difference between the circulations (and also areal contraction rates) at broadside and transitional azimuths (Fig. 7), thus demonstrating that at short range, both circulations and areal contraction rates are relatively insensitive to the difference between the broadside and transitional azimuthal spacings.

To find out the range-dependence of signatures on a simulated PAR, we changed the range of the simulated Doppler velocity patterns of the convergent vortex flow from 25 km to 75 km. Beam spreading reduces the velocity maximum in the core region. The locations of the velocity peaks in Figs. 8c, f indicate that the apparent core diameter is slightly greater than the model core diameter (blue dashed circle), owing to the range degradation. The magnitudes of the peaks are significantly lower at transitional azimuth (Table 1). Observed areal contraction rates straddling the 2.5-km core radius are more accurately measured than observed circulations (Fig. 9) because radial resolution is finer than azimuthal resolution (except very close to the radar). At 25-km range, circulation and areal contraction rate asymptote to approximately one half the actual values. However, the asymptotes are reached at larger radii owing to the degradation of Doppler velocity peaks.

7. CONCLUSIONS AND FUTURE WORK

Our simulated PAR Doppler measurements of convergent vortex flows allow us to examine the effects of range and azimuthal variations on the single-Doppler circulations and areal contraction rates. Contraction rates are more accurately measured than circulations because radial resolution is finer than azimuthal resolution (except very close to the radar). For an idealized mesocyclone, the circulation around a concentric circle surrounding the core is a slightly better measure of vortex strength than rotational velocity. The observed radius of the mesocyclone fluctuates with range. Circulation is relatively insensitive to range and changes in azimuthal beamwidth between the broadside (0^o) and transitional (45^o) azimuths.

Ward (1972) was the first to realize that a tornado is a narrow intense vortex embedded not in a sink flow of comparable diameter (aside from the flow through the small corner region next to the ground) but in a much wider parent updraft. In further work, we have modelled this flow by using a tornado-scale core radius for tangential velocity and a mesocyclone-scale one for radial velocity in (6.2a, b). For the idealized tornado, the circulation around a circle is a more useful measure of vortex strength than rotational velocity. Compared to rotational velocity, circulation declines far more slowly with increasing range and azimuthal spacing, and is less sensitive to whether the tornado is on grid radials or midway between them.

We will continue this work by further investigating the effects of range and azimuth variations on observed circulations and areal contraction rates of convergent mesocyclones and tornadoes of various sizes and strengths. Additionally, we will examine the effects of noisy Doppler velocity data on the calculated circulations and areal contraction rates for different ranges and azimuthal beamwidths.

Lastly, we plan to test our above methods both on simulated PAR Doppler velocity data and on actual NOAA National Weather Radar Testbed Phased-Array Radar located in Norman. We will report on its success or failure compared to other methods [e.g., linear least squares derivatives (LLSD) method for calculating azimuthal shear developed by Smith and Elmore (2004)] for detecting and measuring vortices.

Acknowledgments. The authors thank T. Schuur of NSSL for providing his helpful comments.

REFERENCES

Bourke, P., 1987: CONREC – A Contouring Subroutine. [Available online at http://paulbourke.net/papers/conrec/].

Brown, R. A., and V. T. Wood, 2012: Simulated vortex detection using a four-face phased-array Doppler radar. *Wea. Forecasting,* **27,** 1598-1603.

Davies-Jones, R., 1993: Useful formulas for computing divergence, vorticity, and their errors from three or more stations. *Mon. Wea. Rev.,* **121,** 713-725.

Davies-Jones, R., and G. J. Stumpf, 1997: On the detection and measurement of circulation and areal expansion rate with WSR-88D radars. Preprints, *28th Conf. on Radar Meteorology,* Austin, TX, Amer. Meteor. Soc., 9A.2, 313-314.

Davies-Jones, R. P., and V. T. Wood, 2006: Simulated Doppler velocity signatures of evolving tornado-like vortices. *J. Atmos. Oceanic Technol.,* **23,** 1029-1048.

Doviak, R. J., and D. S. Zrnić, 1993: *Doppler Radar and Weather Observations.* 2nd ed. Academic Press, 562 pp.

Heinselman, P. L., and S. M. Torres, 2011: High-temporal-resolution capabilities of the National Weather Radar Testbed phased-array Radar. *J. Appl. Meteor. Climatol.,* **50,** 579–593.

Heinselman, P. L., D. L. Priegnitz, K. L. Manross, T. M. Smith, and R. W. Adams, 2008: Rapid sampling of severe storms by the National Weather Radar Testbed phased array radar. *Wea. Forecasting,* **23,** 808–824.

Hess, S. L., 1959: *Introduction to Theoretical Meteorology.* Holt, Rinehart and Winston, 362 pp.

Hildebrand, F. B., 1962: *Advanced Calculus for Applications*, Prentice-Hall, 646 pp.

Kreyszig, E., 1972: *Advanced Engineering Mathematics* (3rd ed.), Wiley, 866 pp.

Machado, L. A. T., and H. Laurent, 2004: The convective system area expansion over Amazonia and its relationships with convective system life duration and high-level wind divergence. *Mon. Wea. Rev.,* **132,** 714-725.

Mack, R. A., and D. P. Wylie, 1982: An estimation of the condensation rates in three severe storm systems from satellite observations of the convective mass flux. *Mon. Wea. Rev.,* **110,** 725-744.

National Academies, 2008: *Evaluation of the Multifunction Phased Array Radar Planning Process.* National Academy Press, 79 pp.

Peace, R. L., Jr., R. A. Brown, and H. G. Camnitz, 1969: Horizontal motion field observations with a single Doppler radar. *J. Atmos. Sci.,* **26,** 1096-1103.

Petterssen, S., 1956: *Weather Analysis and Forecasting, Vol. I, 2nd ed.,* New York, McGraw-Hill Book Co. Inc., 428 pp.

Rankine, W. J. M., 1882: *A Manual of Applied Physics.* 10th ed., Charles Griff and Co., 663 pp.

Saucier, W. J., 1955: *Principles of Meteorological Analysis.* University of Chicago Press, 438 pp.

Sikdar, D. N., V. E. Suomi, and C. E. Anderson, 1970: Convective transport of mass and energy in severe storms over the United States – An estimate from a geostationary altitude. *Tellus,* **5,** 521-532.

Smith, T. M., and K. L. Elmore, 2004: The use of radial velocity derivatives to diagnose rotation and divergence. Preprints, *11th Conf. on Aviation, Range and Aerospace,* Hyannis, MA, Amer. Meteor. Soc., P5.6. [Available online at http://ams.confex.com/ams/pdfpapers/81827.pdf.]

Torres, S., R. Adams, C. Curtis, E. Forren, I. Ivić, D. Priegnitz, J. Thompson, and D. Warde, 2013: New weather-surveillance capabilities for NSSL's phased-array radar. Preprints, *29th Conf. on Environmental Information Processing Technologies*, Amer. Meteor. Soc., Austin, TX, 8.2.

Wallace, J. M., and Hobbs, P. V., 1977: *Atmospheric Science: An Introductory Survey.* Academic Press, New York, 467 pp.

Ward, N. B., 1972: The exploration of certain features of tornado dynamics using a laboratory model. *J. Atmos. Sci.,* **29,** 1194-1204.

Weber, M. E., J. Y. N. Cho, J. S. Herd, J. M. Flavin, W. E. Benner, and G. S. Torok, 2007: The next-generation multimission U. S. surveillance radar network. *Bull. Amer. Soc.,* **88,** 1739-1751.

Zrnić, D. S., J. F. Kimpel, D. E. Forsyth, A. Shapiro, G. Crain, R. Ferek, J. Heimmer, W. Benner, T. J. McNellis, and R. J. Vogt, 2007: Agile beam phased array radar for weather observations. *Bull. Amer. Soc.,* **88,** 1753–1766.

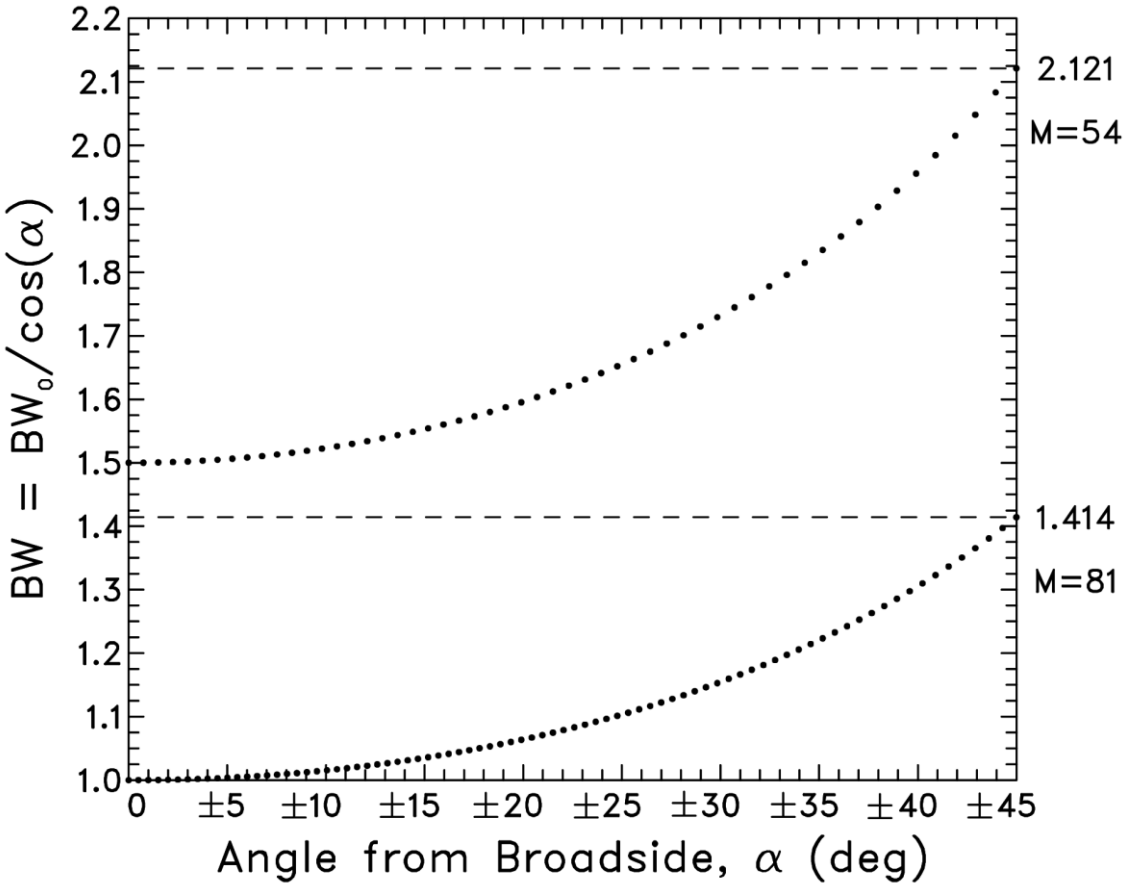

FIG. 1. Azimuthal variation (dotted curve) of beamwidth (BW) and off-broadside azimuth interval for two different broadside beamwidths (BW_o of 1.0° and 1.5°), when using only single flat-face phased-array antenna. M represents the half of total number of grid azimuths per face and is calculated from Eq. (3.7). At BW_o, M=0. Values of BW = 1.414 and 2.121 occur at the transitional (off-broadside) azimuths of ±45°.

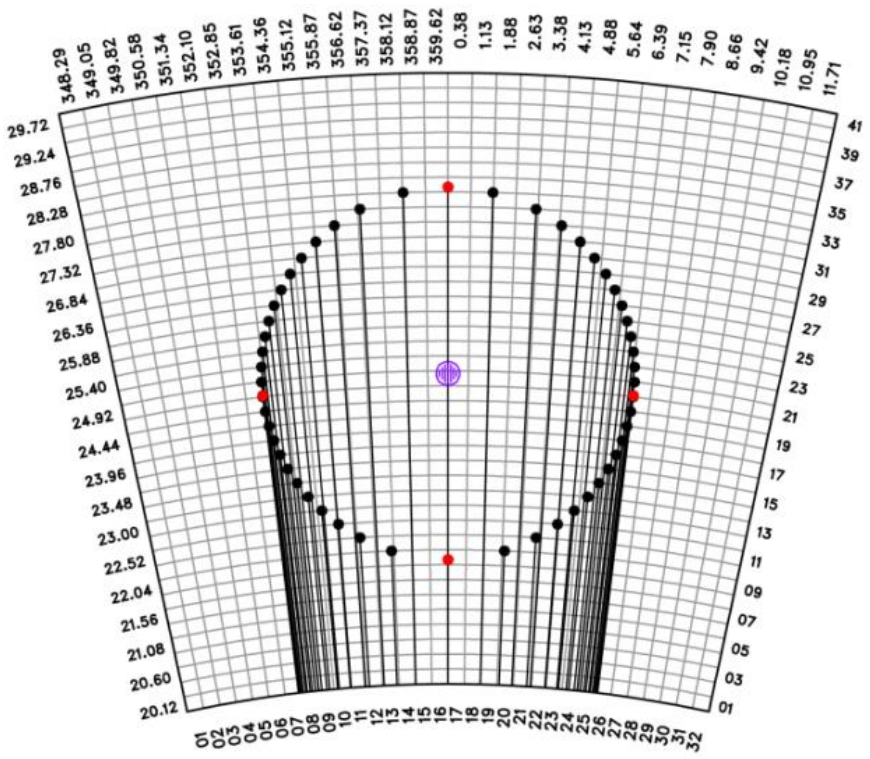

FIG. 2. The interpolation (black) points relative to a simulated PAR site represent the circle around which the circulation and areal contraction rate are calculated. Four extra red dots are added to the interpolation points on the circle. Magenta dot represents the center of the circle at 25 km north of the PAR. Velocity data point is located at the center of gray grid. Variable azimuths are indicated at top. Range increment is 240 m.

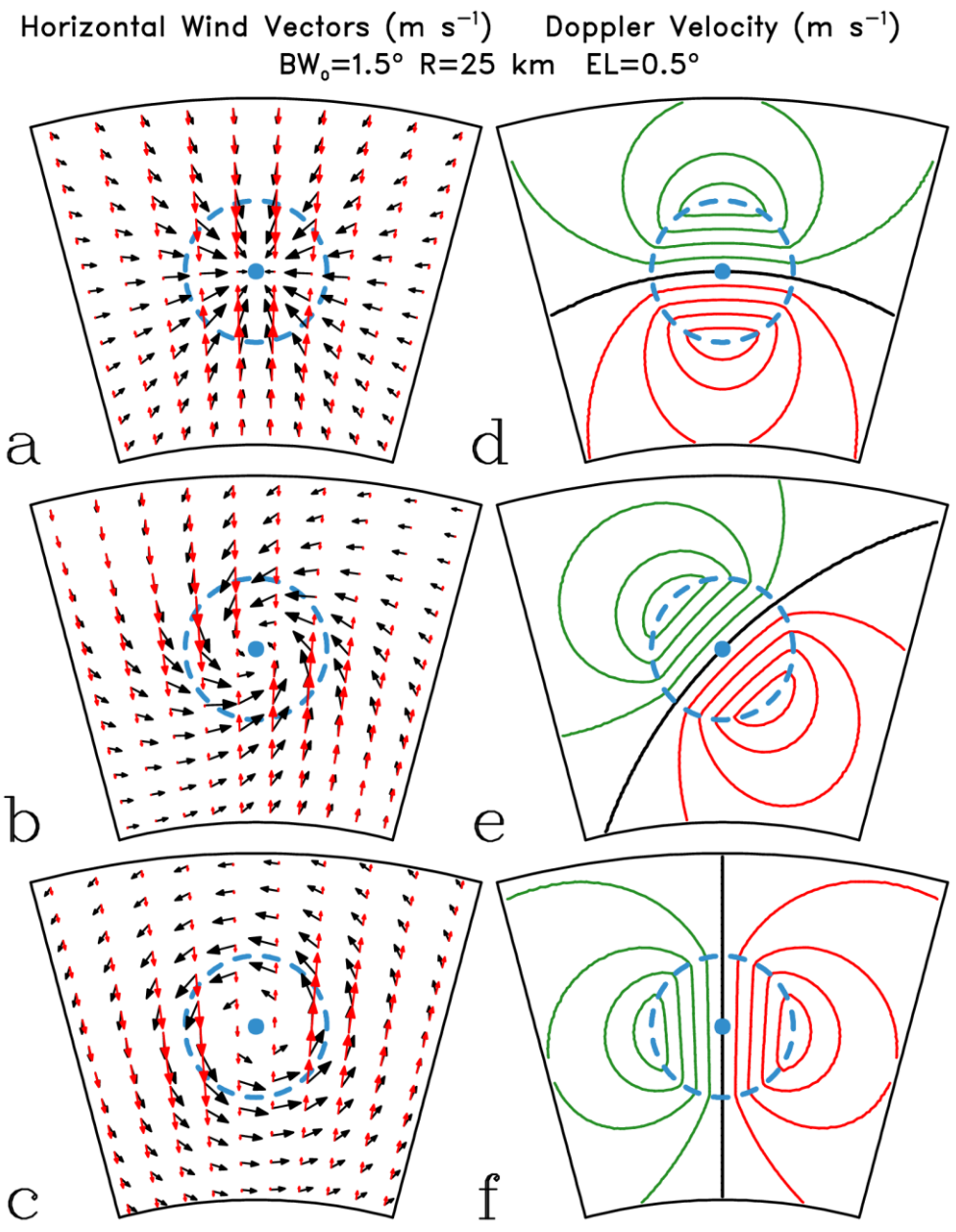

FIG. 3. Simulated, storm-relative horizontal (black) and Doppler (red) wind vectors with (a) convergent flow, (b) combined convergent and rotational flows, and (c) rotational flow are indicated at 0.5°-elevation angle. Red wind vector represents a simulated Doppler velocity component that corresponds to the black horizontal wind vector. (d)-(f) Doppler velocity contours correspond to black wind vectors shown in (a)-(c). Positive (negative) Doppler velocities represent flow away from (toward) the radar, shown by red (green) contours with contour interval of 5 m s^{-1}. Zero Doppler velocity contour (black) represents flow perpendicular to the radar viewing direction. In all panels, a blue Doppler signature center is located at 25 km north of the radar. Blue, dashed circle represents an axisymmetric Rankine core diameter ($2R_x$) of 5 km with its maximum radial (U_x) and tangential (V_x) velocities.

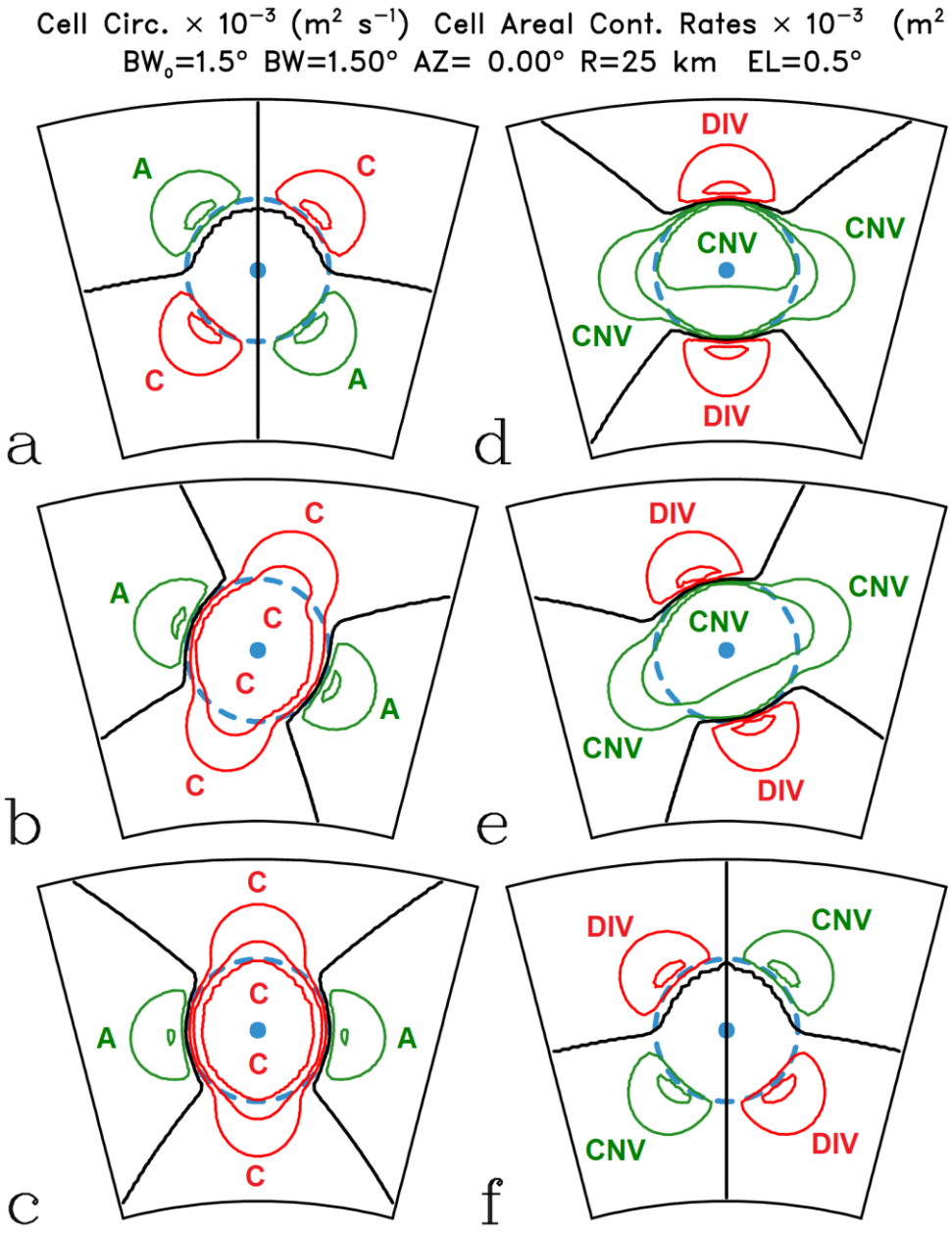

FIG. 4. Calculated cell circulations in (a)-(c) and cell areal contraction rates in (d)-(f) are plotted. Positive (red) and negative (green) contours with zero (black) contours are indicated with contour interval of 0.25 m^2 s^{-1}. Red bold letter C stands for Doppler cyclonic shear; green bold letter A for Doppler anticyclonic shear; green bold word CNV for Doppler convergence; and red bold word DIV for Doppler divergence, as they correspond to Doppler wind vectors (red) in Figs. 3a-c. A blue Doppler signature center is located at 25 km north of a simulated Doppler radar. Blue, dashed circle represents an axisymmetric Rankine core diameter ($2R_x$) of 5 km with its maximum radial (U_x) and tangential (V_x) velocities.

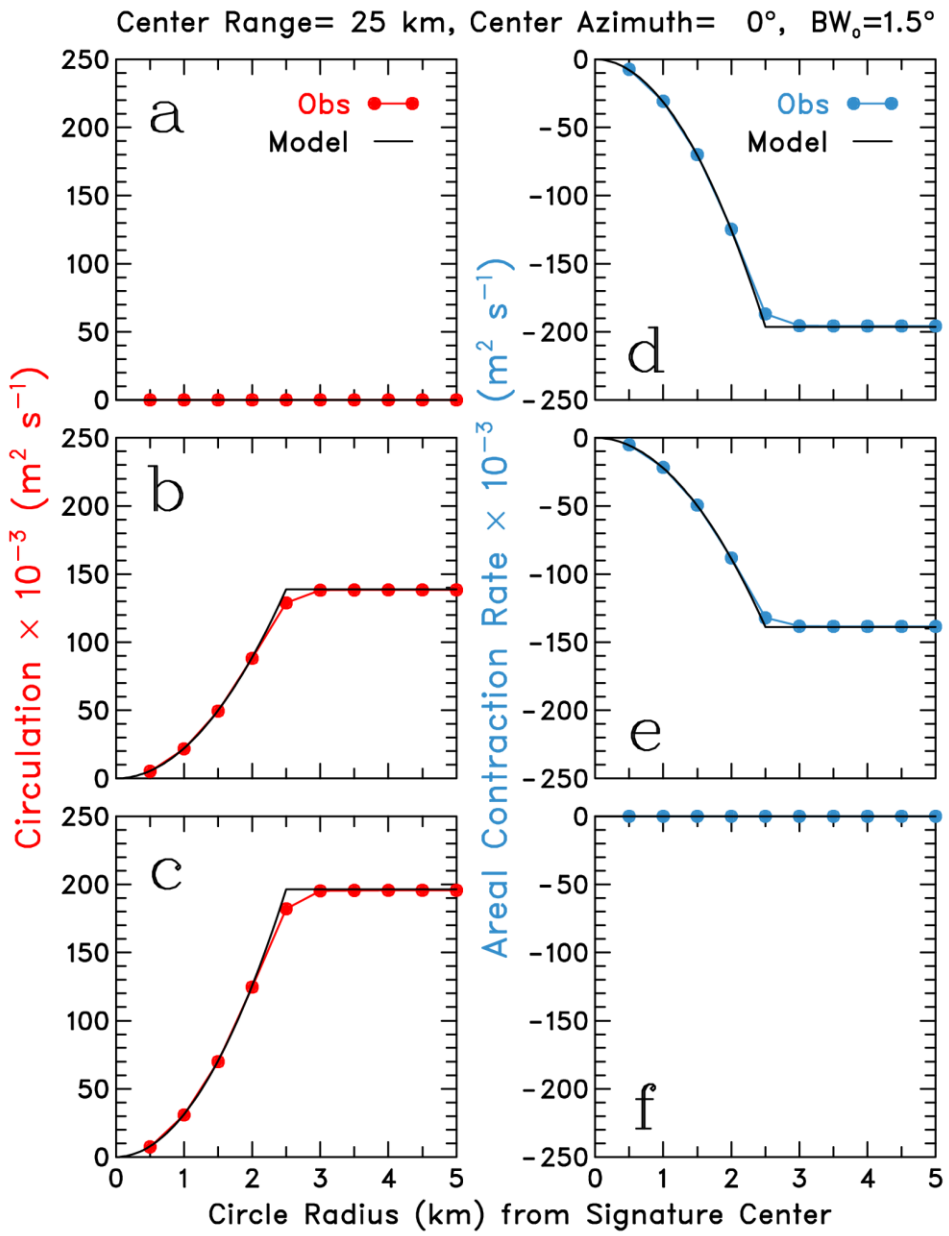

FIG. 5. Observed circulations [red dotted curves in (a)-(c)] and areal contraction rates [blue dotted curves in (d)-(f)] as a function of circle radius from the signature center are calculated from Eqs. (4.10) and (5.8), respectively. Model circulations and areal contraction rates are indicated by black curves. The signature center passing through the broadside azimuth of 0° is located at 25 km north of the radar.

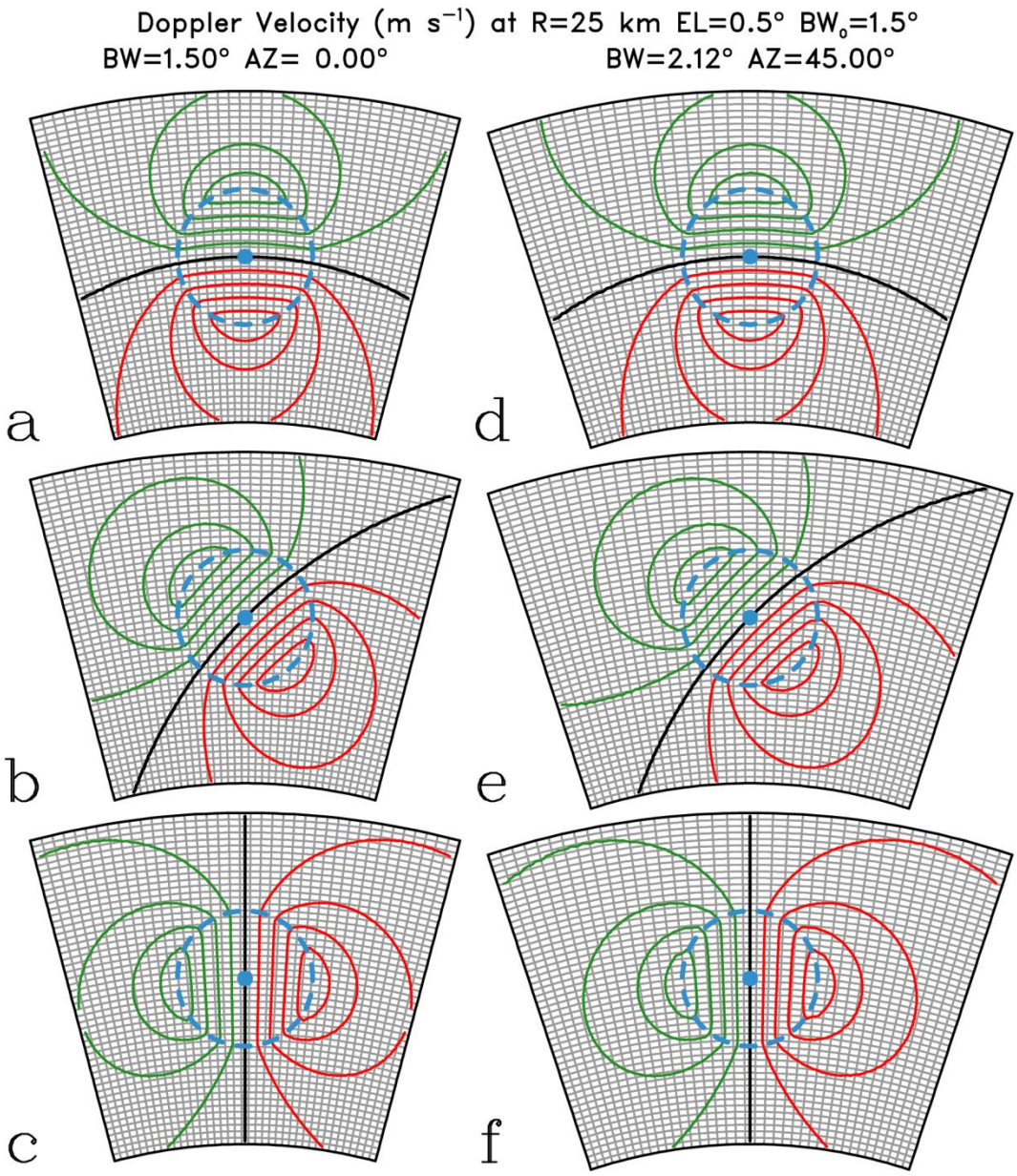

FIG. 6. Single-Doppler velocity patterns associated with the flow fields in FIG. 3a-c at center azimuth of (a)-(c) 0° and (d)-(f) 45° passing through the signature center. Positive (negative) mean Doppler velocities represent flow away from (toward) the radar, shown by red (green) contours with contour interval of 5 m s^{-1}. Zero Doppler velocity contour (black) represents flow perpendicular to the radar viewing direction. In all panels, blue Doppler signature center is located at 25 km north of the radar. Blue, dashed circle represents an axisymmetric Rankine core diameter ($2R_x$) of 5 km with its maximum radial (U_x) and tangential (V_x) velocities. A mean Doppler velocity value is represented by a uniformly (gray) range bin that extends 240 m in range and varying azimuths between two gray radials. A grid data is located at the midpoint of the bin.

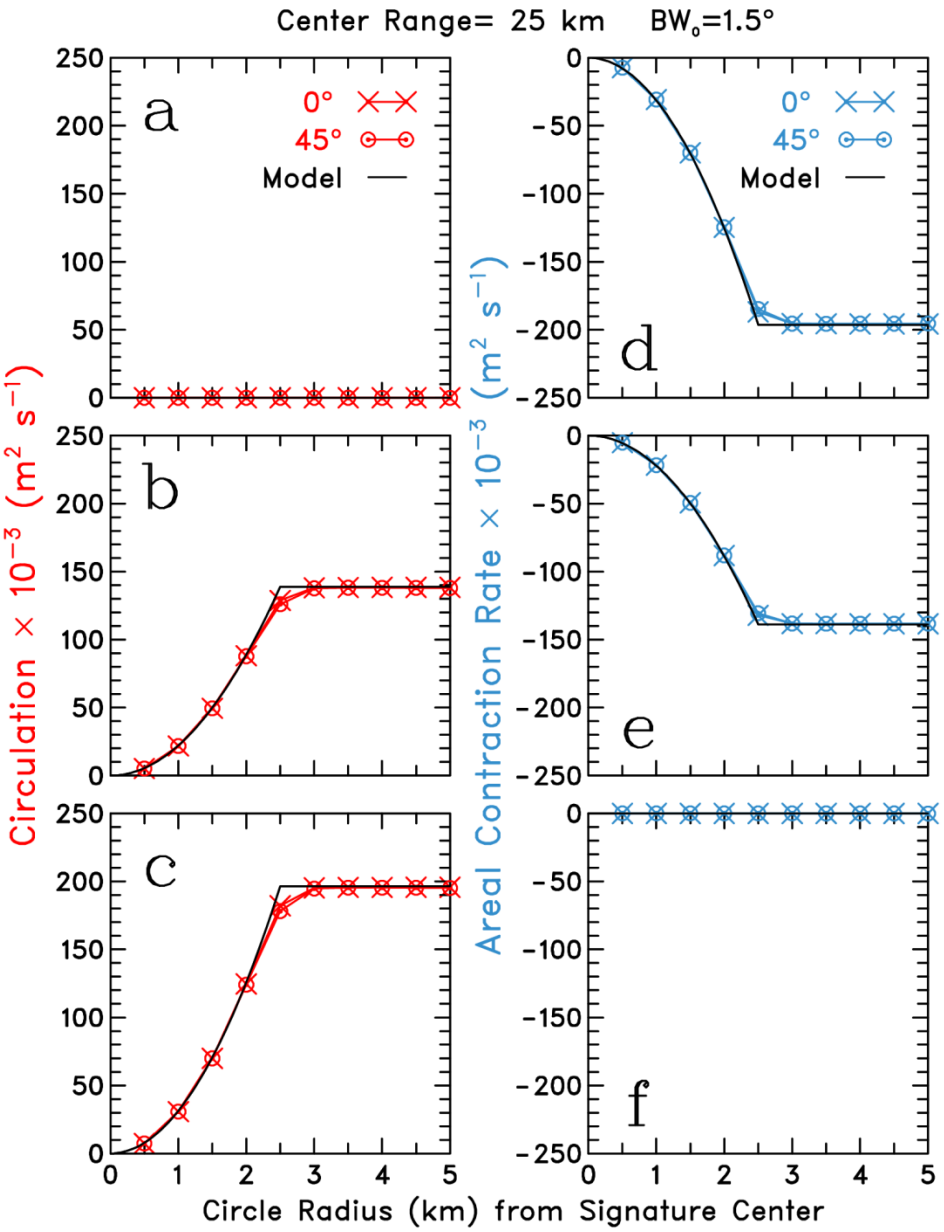

FIG. 7. Same as FIG. 5, except that the × and ○ curves, respectively, represent the observed circulation and areal contraction rate values as a function of circle radius from the signature center when the center is passing through the broadside (0^o) and transitional (45^o) azimuths.

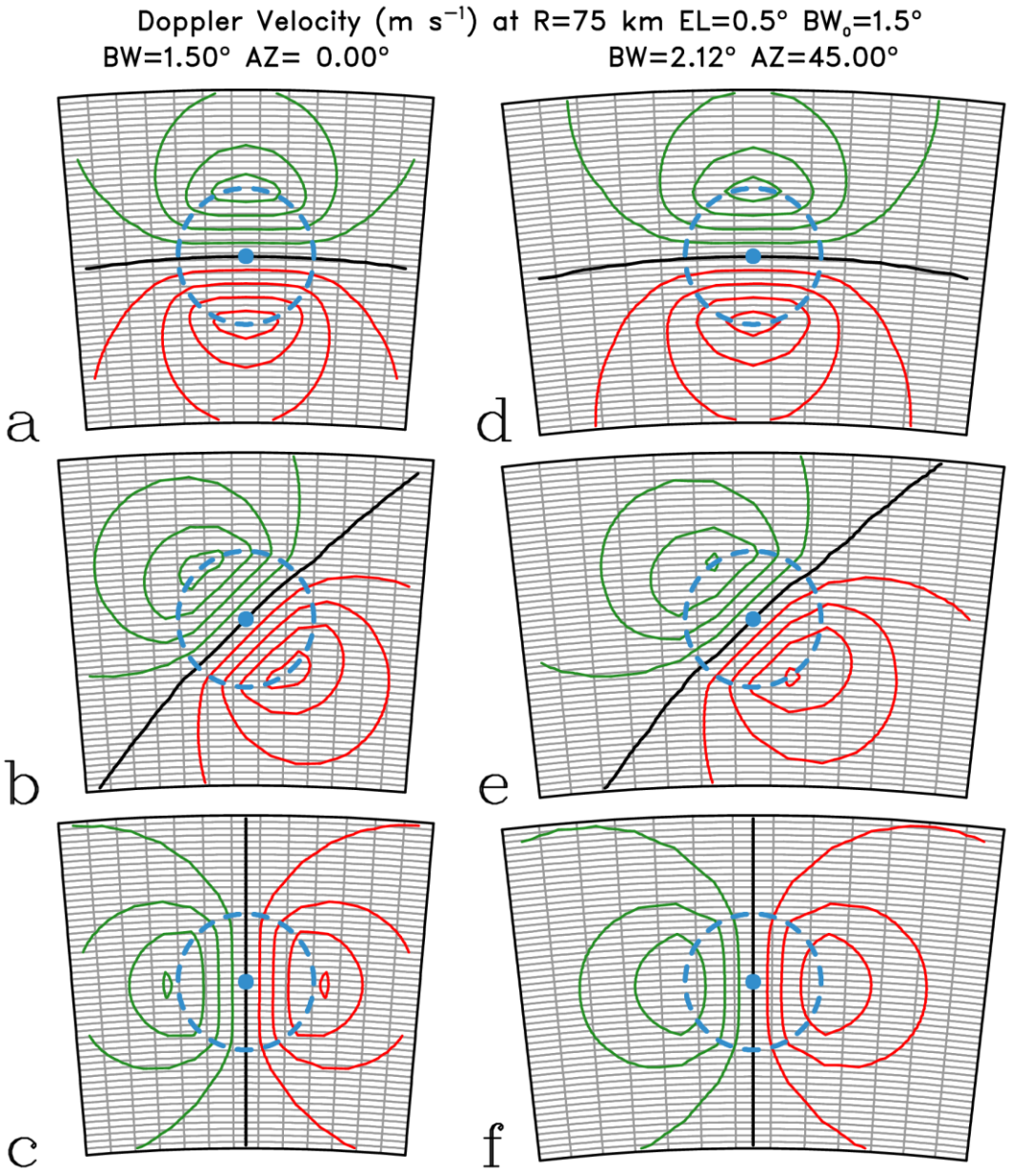

FIG. 8. Same as FIG. 6, except that the signature centers are located at 75 km north of the radar.

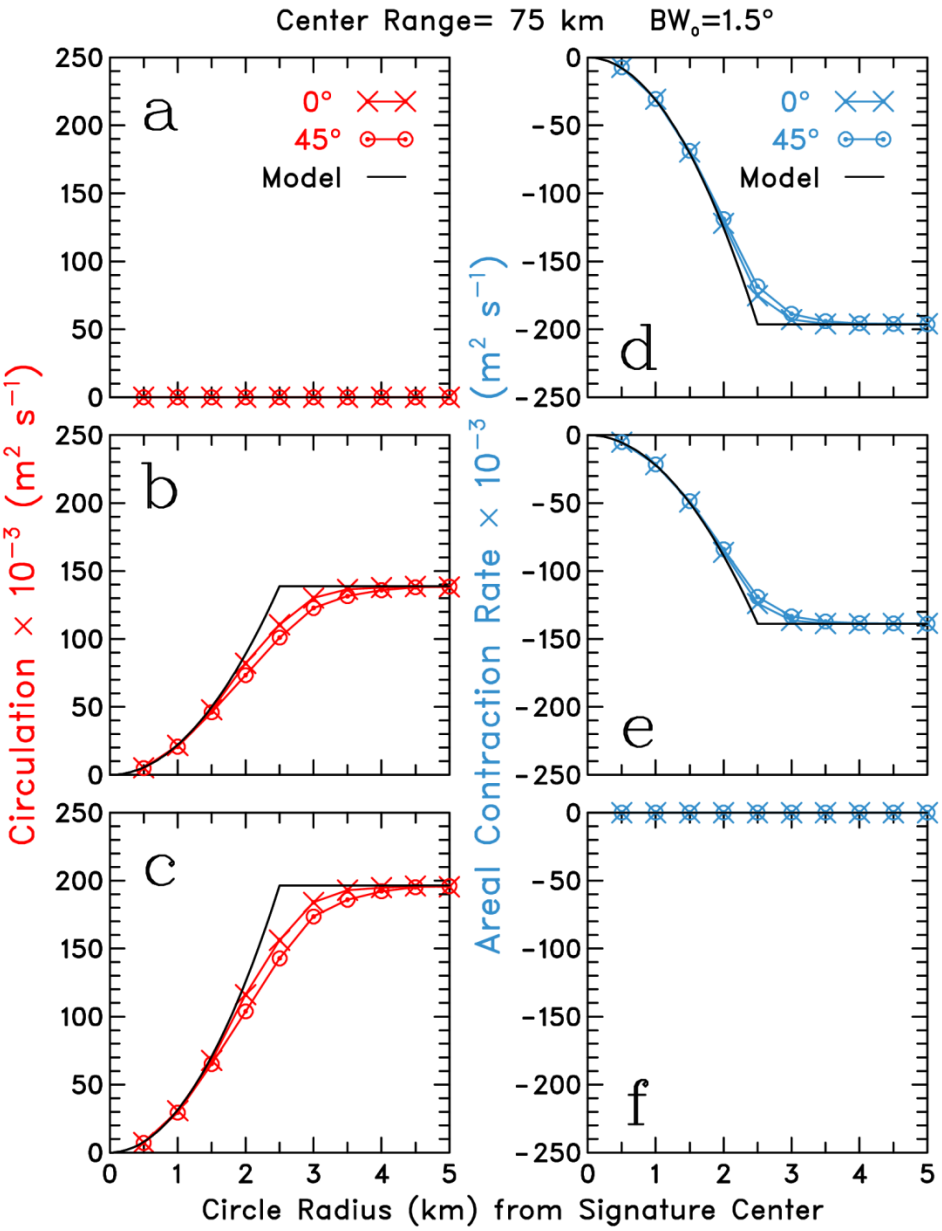

FIG. 9. Same as FIG. 7, except that the signature centers are located at 75 km north of the radar.

TABLE 1. Inbound (V_{in}) and outbound (V_{out}) Doppler velocity peaks, Doppler velocity difference ($\Delta V = V_{out} - V_{in}$) between the two peaks in the characteristic velocity couplet, and ratios of ΔV with simulated (a) and (d) convergent flows, (b) and (e) combined convergent and rotational flows, and (c) and (f) rotational flows as a function of broadside and off-broadside azimuth angles of 0^o and 45^o, respectively, and ranges of 25 and 75 km for $BW_o = 1.5^o$ in the corresponding figures.

Broadside AZ = 0^o				*Off-Broadside AZ=45^o*				
Fig. #	V_{in}	V_{out}	ΔV	*Fig. #*	V_{in}	V_{out}	ΔV	*Ratios*
6a	-23.99	23.98	47.97	6d	-23.96	23.95	47.91	1.00
6b	-23.66	23.89	47.55	6e	-23.41	23.52	46.93	0.99
6c	-23.26	23.28	46.54	6f	-22.91	22.91	45.82	0.98
8a	-23.48	23.48	46.96	8d	-22.70	22.72	45.42	0.97
8b	-21.58	21.63	43.21	8e	-20.60	20.72	41.32	0.96
8c	-20.38	20.38	40.76	8f	-19.62	19.62	39.24	0.96